Dominant-Current Deep Learning Scheme for Electrical Impedance Tomography

Zhun Wei, Dong Liu, and Xudong Chen

Abstract*—*Objective: **Deep learning has recently been applied to electrical impedance tomography (EIT) imaging. Nevertheless, there are still many challenges that this approach has to face, e.g., targets with sharp corners or edges cannot be well recovered when using circular inclusion training data. This paper proposes an iterative-based inversion method and a convolutional neural network (CNN)-based inversion method to recover some challenging inclusions such as triangular, rectangular, or lung shapes, where the CNN-based method uses only random circle or ellipse training data.** ***Methods:*** **First, the iterative method, i.e., bases-expansion subspace optimization method (BE-SOM), is proposed based on a concept of induced contrast current (ICC) with total variation regularization. Second, the theoretical analysis of BE-SOM and the physical concepts introduced there motivate us to propose a dominant-current deep learning scheme (DC-DLS) for EIT imaging, in which dominant parts of ICC are utilized to generate multi-channel inputs of CNN.** ***Results:*** **The proposed methods are tested with both numerical and experimental data, where several realistic phantoms including simulated pneumothorax and pleural effusion pathologies are also considered.** ***Conclusions and Significance:*** **Significant performance improvements of the proposed methods are shown in reconstructing targets with sharp corners or edges. It is also demonstrated that the proposed methods are capable of fast, stable, and high-quality EIT imaging, which is promising in providing quantitative images for potential clinical applications.**

***Index Terms*—Electrical impedance tomography, induced contrast current, subspace optimization method, deep learning.**

I. Introduction

ELECTRICAL impedance tomography (EIT) is a non-invasive technique to visualize living tissues of the body for biomedical imaging applications [1]–[5]. In EIT, by attaching conducting surface electrodes around the body and applying small alternating currents, the voltages on the electrodes are recorded and used to reconstruct conductivities of tissues or organs in the body. EIT is clinically useful in chest imaging to monitor lung functions since the conductivities of lung tissues are much lower than those of other soft tissues within the thorax, where it has been validated in obtaining information of pathologies [6], [7], such as pleural effusion and pneumothorax. Although EIT is a powerful and promising technology for its radiation-free, low-cost and portable properties, reconstructing electrical properties from EIT is a challenging inverse problem due to its nonlinear and highly ill-posed properties and sensitivities to measurement noise and modeling errors [3], [8], [9].

This work was supported by the National Research Foundation, Prime Minister's Office, Singapore under its Competitive Research Program (CRP Award No. NRF-CRP15-2015-03). Dong Liu was supported by the National natural science foundation of China under Grant No. 61871356 and Anhui Provincial Natural Science foundation under Grant 1708085MA25.

Z. Wei and X. Chen are with Department of Electrical and Computer Engineering, National University of Singapore, 4 Engineering Drive 3, Singapore 117583, Singapore (e-mail: elechenx@nus.edu.sg). D. Liu is with CAS Key Laboratory of Microscale Magnetic Resonance and Department of Modern Physics, University of Science and Technology of China (USTC), Hefei 230026, China, Hefei National Laboratory for Physical Sciences at the Microscale, USTC, China, and also with Synergetic Innovation Center of Quantum Information and Quantum Physics, USTC, China

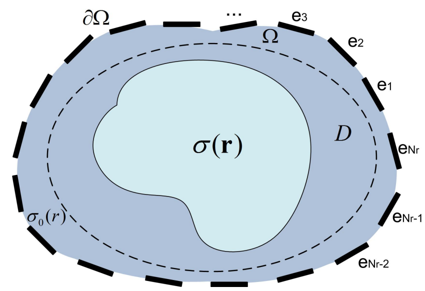

Fig. 1. A typical schematic of EIT problem with a two dimensional domain, where a total number of N_r electrodes are attached on the boundary $\partial\Omega$. The dash line denotes the boundary of domain of interest (DOI) D, within which all materials that are different from the background materials, referred to as inclusions, are located.

Iterative optimization methods are typically used to solve EIT problem with regularizations, such as total variation based algorithms [9], [10], boundary element-based methods [11], variationally constrained numerical methods [12], and subspace-based optimization methods (SOM) [13], [14]. Besides iterative methods, some non-iterative methods have also been proposed, such as the factorization method [15], [16], the Calderóns method [17], [18], and the D-bar algorithm [19]–[21]. Typically, iterative methods with regularizations perform well in the quality of reconstruction but they usually suffer from heavy computational costs and sensitivities to measurement noise and modeling errors [22], [23]. On contrary, non-iterative methods are usually faster than iterative methods but the image qualities are limited. Further, the spatial resolutions of the reconstructed images for both iterative and non-iterative methods are severely limited by the ill-posedness and nonlinearity of EIT problem, which hinders the clinical applicability. To improve the spatial resolution of reconstructed image, one commonly used method is to incorporate spatial *a priori* information of organ boundaries into algorithms [20]. Recently, deep learning has attracted intensive attention for providing promising results for image classification [24]–[26], object detection [27], and segmentation [28], [29]. Neural networks with regression features have also provided impressive results on inverse problems, such as signal denoising [30], deconvolution [31], interpolation [32], and solving ill-posed linear inversion problems [33].

In the first part of this work, a bases-expansion subspace optimization method (BE-SOM) is presented based on a concept of induced contrast current (ICC), where a forward solver with the method of moment (MOM) [34] is proposed for EIT problem under the gap model [35]. A bases-expansion strategy with total variation is also incorporated in BE-SOM to increase the robustness and convergence of the method. In the second part of this work, based on the theoretical analysis and physical concepts presented in BE-SOM, a dominant-current deep learning scheme (DC-DLS) is proposed for EIT imaging, where dominant parts of induced contrast current (ICC) are utilized to generate multi-channel inputs of convolutional neural network (CNN).

Recently, there are also some works which have applied deep learning to EIT imaging, such as [21]. Compared to the work in [21], the advantages of the proposed DC-DLS are threefold: Firstly, different from previous literatures, we start the training from a concept of ICC. Instead of imitating shapes of training data, DC-DLS trains and learns the mathematical relationship between ground-truth conductivities and the conductivities that are obtained from the dominant part of ICC, which describes the EIT physics within the domain of interest (DOI) in the natural pixel bases. Thus, DC-DLS is able to reconstruct complex inclusions, such as triangular and lung targets, when the network is trained with only random circle or ellipse inclusion data. Secondly, instead of using original U-net architecture in [29], skip connections and batch normalization are further added to the U-net structure, where skip connections are used to mitigate the vanishing gradient problem [33], [36] and batch normalization (BN) is used to alleviate the internal covariate shift during training [37]. Thirdly, we have also introduced a multiple-channel scheme (MCS) in DC-DLS to modify U-net, which enlarges the data set and increases robustness by data augmentations in DC-DLS [38].

It is worth introducing the notations used throughout the paper. We use $\overline{\overline{X}}$ and $\overline{X}$ to denote the matrix and vector of the discretized parameter X, respectively. Furthermore, the superscripts $*$, T, and H denote the complex conjugate, transpose, and conjugate transpose of a matrix or vector, respectively. Finally, we use $||\cdot||_F$ to denote Frobenius norm.

II. Forward Solver

In this paper, as depicted in Fig. 1, we consider a typical two-dimensional chest-shaped domain Ω, where the boundary of domain Ω can be obtained from optical cameras in practice. Actually, domain Ω can be of arbitrary shape, and we choose the one in Fig. 1 as an example to present our method. Some inclusions with conductivity of $\sigma(r)$ are embedded in a DOI D interior to domain Ω, where the background is some material with the conductivity of $\sigma_0(r)$. There are a total number of N_r electrodes attached on the boundary $\partial\Omega$ which are labeled as $e_1, e_2, ..., e_{N_r}$ in Fig. 1, where a total number of N_i excitations of current are injected from the electrodes.

The Neumann boundary value problem in EIT can be described as the following equations under gap model [35]:

$$\nabla\cdot[\sigma(r)\nabla\mu]=0 \quad r\in\ \Omega, \tag{1}$$

$$\sigma_0(r)\frac{\partial\mu}{\partial\nu}=J_q/|e_q| \quad r\in\ e_q, q=1,2,...,N_r, \tag{2}$$

$$\sigma_0(r)\frac{\partial\mu}{\partial\nu}=0 \quad r\in\partial\Omega\bigcap r\notin e_q, q=1,2,...,N_r, \tag{3}$$

where μ is the electrical potential in domain Ω and ν is the outer normal direction on the boundary $\partial\Omega$. J_q and $|e_q|$ are the current injected into the qth electrode and the length of the qth electrode, respectively. Further, conservation of charge is included with $\sum\limits_{q=1}^{N_r} J_q = 0$, and a condition on the voltages to specify the ground or zero potential is also defined as $\sum\limits_{q=1}^{N_r}\int_{e_q}\mu ds=0$.

Since the partial differential equation (1) can further be formulated as $\nabla\cdot\{[\sigma_0(r)+\sigma(r)-\sigma_0(r)]\nabla\mu\}=0$, it is easy to obtain

$$\nabla\cdot[\sigma_0(r)\nabla\mu]=-\rho_{in} \tag{4}$$

with the contrast source $\rho_{in}=\nabla\cdot\{[\sigma(r)-\sigma_0(r)]\nabla\mu\}$, where μ in (4) can be understood as the potential produced by the contrast source ρ_{in} in the background media. It is noted that the proposed forward solver applies to background media with arbitrary inhomogeneous materials with conductivity $\sigma_0(r)$. For sake of simplicity, we choose a homogeneous background σ_0 for the purpose of ease in presenting our model and its physical insight in this paper.

To solve (4), the Green's function $G(r,r')$ in background medium is defined and it satisfies the following differential equations [39]:

$$\nabla\cdot[\sigma_0\nabla G(r,r')]=-\delta(r-r'), \tag{5}$$

$$\sigma_0\frac{\partial G}{\partial\nu}=-\frac{1}{|L_t|} \quad r\in\ e_q, q=1,2,...,N_r, \tag{6}$$

$$\sigma_0\frac{\partial G}{\partial\nu}=0 \quad r\in\partial\Omega\bigcap r\notin e_q, q=1,2,...,N_r, \tag{7}$$

where $\delta(r-r')$ and $|L_t|$ are the Dirac delta function and the total length of all electrodes, respectively. Here, r and r' are the field point and source point in domain Ω, respectively.

With Green's Theorem [39], it is easy to obtain the solution of Poisson equation (4) as:

$$\mu=\mu^0(r)+\int_\Omega-\nabla'G(r,r')\cdot\{[\sigma(r')-\sigma_0]\nabla'\mu(r')\}dr', \tag{8}$$

where $\mu^0(r)$ is the voltage when there is no inclusion presented in the domain Ω. Noting that the contrast $\sigma(r')-\sigma_0$ is nonzero only for $r'\in$ DOI D, we change the integral domain from Ω to D. Taking gradient on both side of (8), we have the following self-consistent equation:

$$E^t=E^0(r)+\int_D-\nabla\{\nabla'G(r,r')\cdot[(\sigma(r')-\sigma_0)E^t(r')]\}dr' \tag{9}$$

where electric field $E^t=-\nabla\mu$ and $E^0=-\nabla\mu^0$.

To solve (9), we use the method of moment (MOM) with the pulse basis function and the delta testing function to discretize the DOI into M subunits [34], and the centers of subunits are located at $\overline{r}_1, \overline{r}_2, \ldots, \overline{r}_M$. The total electric field at the center of subunits $\overline{E}^t_p(\overline{r}_m)$ can be expressed as

$$\overline{E}^t_p(\overline{r}_m) = \overline{E}^0_p(\overline{r}_m) + \sum_{n=1}^{M} \overline{\overline{G}}_D(\overline{r}_m, \overline{r}_n) \cdot \overline{\overline{\xi}}_n \cdot \overline{E}^t_p(\overline{r}_n), \quad (10)$$

where p represents the pth injection of current with $p = 1, 2, \ldots, N_i$, and $\overline{E}^0_p(\overline{r}_m)$ is the electric field in the background. According to (8), the polarization tensor $\overline{\overline{\xi}}_n$ is defined as

$$\overline{\overline{\xi}}_n = A_n[\sigma(\overline{r}_n) - \sigma_0]\overline{\overline{I}}_2, \quad (11)$$

where $\overline{\overline{I}}_2$ and A_n are two-dimensional identity matrix and the area of the nth subunit, respectively. Note that the polarization tensor defined in (11) is different from that used in small scatterers [40], [41]. The Green's function $\overline{\overline{G}}_D(\overline{r}_m, \overline{r}_n)$ is characterized as $\overline{\overline{G}}_D(r, r') \cdot \overline{d} = -\nabla[\nabla' G(r, r') \cdot \overline{d}]$ for an arbitrary dipole $\overline{d}$. Due to the irregular boundary shape, $\overline{\overline{G}}_D(\overline{r}_m, \overline{r}_n)$ does not have analytical solution, which is computed with numerical software and saved as a library.

If we define the ICC $\overline{J}(\overline{r}_n)$ in the nth subunit as

$$\overline{J}(\overline{r}_n) = \overline{\overline{\xi}}_n \cdot \overline{E}^t_p(\overline{r}_n), \quad (12)$$

and write (10) in a vectorized version as:

$$\overline{E}^t_p = \overline{E}^0_p + \overline{\overline{G}}_D \cdot \overline{J}_p, \quad (13)$$

then the vectorized version of (13) is written as

$$\overline{J}_p = \overline{\overline{\xi}} \cdot [\overline{E}^0_p + \overline{\overline{G}}_D \cdot \overline{J}_p], \quad (14)$$

where $\overline{J}_p$ is a $2M$-dimensional vector

$$\overline{J}_p = [J^x_p(\overline{r}_1), J^x_p(\overline{r}_2), ..., J^x_p(\overline{r}_M), J^y_p(\overline{r}_1), J^y_p(\overline{r}_2), ..., J^y_p(\overline{r}_M)]^T \quad (15)$$

Here, $J^x_p(\overline{r}_M)$ and $J^y_p(\overline{r}_M)$ are x and y component of ICC at $\overline{r}_M$ for the pth injection of current, respectively. $\overline{\overline{G}}_D$ is a $2M \times 2M$ matrix $[\overline{\overline{G}}_{xx}, \overline{\overline{G}}_{xy}; \overline{\overline{G}}_{yx}, \overline{\overline{G}}_{yy}]$, in which each sub-matrix is of size $M \times M$. $\overline{\overline{G}}_{xx}(m,n)$ and $\overline{\overline{G}}_{xy}(m,n)$ are computed as the x component of electric field at $\overline{r}_m$ due to a unit x-oriented and y-oriented dipole placed at $\overline{r}_n$, respectively. $\overline{\overline{G}}_{yx}$ and $\overline{\overline{G}}_{yy}$ are evaluated in a similar way. The polarization tensor $\overline{\overline{\xi}}$ is a $2M \times 2M$ diagonal matrix with the $2M$ diagonal elements being $[\xi_1, \xi_2, ..., \xi_m, ..., \xi_M, \xi_1, \xi_2, ..., \xi_M]$, where ξ_m is calculated by

$$\xi_m = A_m[\sigma(\overline{r}_m) - \sigma_0] \quad (16)$$

and A_m is the area of the mth subunit.

According to (8), the differential voltage on the boundary $V(r_{\partial\Omega}) = \mu - \mu^0$ can be formulated as

$$V(r_{\partial\Omega}) = \int_D -\nabla' G(r_{\partial\Omega}, r') \cdot \{[\sigma(r') - \sigma_0]\nabla'\mu(r')\} dr', \quad (17)$$

where $r_{\partial\Omega}$ is the position at the boundary $\partial\Omega$. Following the same discretization method in (10), the differential voltage $\overline{V}_p$ at the boundary for pth injection is calculated as

$$\overline{V}_p = \overline{\overline{G}}_\partial \cdot \overline{J}_p, \quad (18)$$

where $\overline{\overline{G}}_\partial(r_{\partial\Omega}, r')$ is characterized as $\overline{\overline{G}}_\partial(r_{\partial\Omega}, r') = \nabla' G(r_{\partial\Omega}, r')$ and $\overline{\overline{G}}_\partial$ is a $N_r \times 2M$ matrix $[\overline{\overline{G}}^x_\partial, \overline{\overline{G}}^y_\partial]$. $\overline{\overline{G}}^x_\partial(q,n)$ and $\overline{\overline{G}}^y_\partial(q,n)$ are calculated as the potential on the boundary node $\overline{r}_q$ due to a unit x-oriented and y-oriented dipole placed at $\overline{r}_n$, respectively. Here, $\overline{r}_q$ denotes the central position of the qth electrode.

In the forward solver, (14) describes the electromagnetic interactions in domain Ω and is usually referred to as the state equation. Equation (18) describes the voltage collected on electrodes produced by the ICC and is referred to as the data equation. In the following section, both BE-SOM and DC-DLS are proposed based on state and data equations.

In this paper, COMSOL Multiphysics software (2D AC/DC module) has been used to verify the proposed forward solver, where various tests show that numerical results calculated by the proposed forward model agree well with the simulation results in COMSOL. It is noted that, for complex-valued admittivities γ or three-dimensional (3D) problems, the proposed framework in this paper still works. For example, to solve complex-valued admittivities, one only needs to replace all the conductivities by complex-valued admittivities $\gamma(r) = \sigma(r) + i\omega\varepsilon(r)$ with ω and $\varepsilon(r)$ being angular frequency and permittivity, respectively.

III. Inversion Methods

A. Bases-Expansion Subspace Optimization Method

In the inverse problem, the conductivity inside the DOI will be reconstructed and consequently inclusions can be identified. It is important to highlight that the parameter to be reconstructed in the proposed inversion model is the contrast $\sigma(r) - \sigma_0(r)$. It is also stressed that the background conductivity $\sigma_0(r)$ is not required to be accurate, since the contrast $\sigma(r) - \sigma_0(r)$ automatically offsets it for the simple reason that

$$\sigma(r) = \sigma_0(r) + [\sigma(r) - \sigma_0(r)]. \quad (19)$$

It is noted that the proposed approach not only allows to reconstruct the contrast, i.e., conductivity change in general difference EIT when the measurement data before the change is available, but also offers a chance to estimate the absolute conductivity distribution when only the data after the change is available ($\sigma_0(r)$ is not known). Specifically, it is done by simulating the data with a conductivity distribution $\sigma_0(r)$, and then compensating $\sigma_0(r)$ to $\sigma(r)$, as shown in (19).

If a singular value decomposition (SVD) is conducted on $\overline{\overline{G}}_\partial$, one can obtain $\overline{\overline{G}}_\partial = \sum_m \overline{u}_m \sigma_m \overline{\nu}^H_m$ with $\overline{\overline{G}}_\partial \cdot \overline{\nu}_m = \sigma_m \overline{u}_m$, $\sigma_1 \geq \sigma_2 \ldots \geq \sigma_{2M} \geq 0$, where the superscript H denotes conjugate transpose of a matrix or vector. By considering orthogonality of the singular vectors, the major part of ICC $\overline{J}^+_p$ spanned by the first L dominant singular values can be uniquely calculated from the data equation (18) with [13], [42]

$$\overline{J}_p^+ = \sum_{j=1}^{L} \frac{\overline{\mu}_j^H \cdot \overline{V}_p}{\sigma_j} \overline{\nu}_j, \tag{20}$$

where $\overline{\mu}_j^H$ denotes the conjugate transpose of the singular vector $\overline{\mu}_j$. Since the first L singular values are larger than the remaining ones, the major part of ICC calculated from (20) are more stable when the measured potential $\overline{V}_p$ is contaminated with noises. Nevertheless, $\overline{J}_p^+$ has missed some information contained in the minor part of ICC $\overline{J}_p^-$ which is spanned by the other $2M - L$ singular vectors, and the actual ICC should be $\overline{J}_p = \overline{J}_p^+ + \overline{J}_p^-$.

To avoid heavy computational cost associated with full SVD of $\overline{\overline{G}}_\partial$ adopted in SOM [13], we only need to calculate the first L singular vectors by a thin-SVD to represent the major part of ICC and at the same time the minor part of ICC $\overline{J}_p^-$ is spanned by Fourier bases $\overline{\overline{F}}$.

In BE-SOM, we divide the optimization processes into S stages, where only the first M_k Fourier bases are used to represent $\overline{J}_p^-$ at the kth stage with k = 1, 2, ..., S. The number of Fourier bases M_k are gradually increased from a small value to $2M$, and the result that is obtained from the kth stage is treated as the initial guess in the $(k+1)$th stage. Specifically, the induced contrast current can be written in the form of

$$\overline{J}_p = \overline{J}_p^+ + \overline{\overline{F}}_{M_k} \cdot \overline{\alpha}_p, \tag{21}$$

where $\overline{\alpha}_p$ is an M_k-dimensional vector to be reconstructed at each stage. Since the proposed model uses the SOM and the gradual expansion of Fourier bases, which is referred to as the BE-SOM, its speed of convergence is significantly increased due to the reduction of unknowns at the early stage of optimizations.

With (21), the residual of data equation (18) is formulated as

$$\Delta_p^d = ||\overline{\overline{G}}_\partial \cdot \overline{J}_p^+ + \overline{\overline{G}}_\partial \cdot \overline{\overline{F}}_{M_k} \cdot \overline{\alpha}_p - \overline{V}_p||^2 \tag{22}$$

and residual of state equation (14) becomes

$$\Delta_p^s = ||\overline{\overline{A}} \cdot \overline{\alpha}_p - \overline{B}_p||^2, \tag{23}$$

in which $\overline{\overline{A}} = \overline{\overline{F}}_{M_k} - \overline{\overline{\xi}} \cdot (\overline{\overline{G}}_D \cdot \overline{\overline{F}}_{M_k})$, and $\overline{B}_p = \overline{\overline{\xi}} \cdot (\overline{E}_p^0 + \overline{\overline{G}}_D \cdot \overline{J}_p^+) - \overline{J}_p^+$. The normalized data-related objective function f_d is defined as

$$f_d(\overline{\alpha}_1, \overline{\alpha}_2, ..., \overline{\alpha}_{N_i}, \overline{\overline{\xi}}) = \sum_{p=1}^{N_i} (\Delta_p^d / |\overline{V}_p|^2 + \Delta_p^s / |\overline{J}_p^+|^2). \tag{24}$$

In BE-SOM, total variation (TV) is also added to regularize the solution with the objective function:

$$f_0(\overline{\alpha}_1, \overline{\alpha}_2, ..., \overline{\alpha}_{N_i}, \overline{\overline{\xi}}) = f_d(\overline{\alpha}_1, \overline{\alpha}_2, ..., \overline{\alpha}_{N_i}, \overline{\overline{\xi}}) + \beta f_{TV}(\overline{\overline{\xi}}), \tag{25}$$

where $\beta > 0$ is the weighting parameter, and

$$\begin{aligned} f_{TV}(\overline{\overline{\xi}}) \quad = \quad & \sum_{a,b=1}^{P-1} \sqrt{|\xi_{a+1,b} - \xi_{a,b}|^2 + |\xi_{a,b+1} - \xi_{a,b}|^2 + \eta^2} \\ & + \sum_{a=1}^{P-1} \sqrt{|\xi_{a+1,P} - \xi_{a,P}|^2 + \eta^2} \\ & + \sum_{b=1}^{P-1} \sqrt{|\xi_{P,b+1} - \xi_{P,b}|^2 + \eta^2} \end{aligned} \tag{26}$$

is a discretized approximation of the TV [43]. Before calculating the TV objective function (26), the polarization tensor $\overline{\overline{\xi}}$ is reshaped to $P \times P$ pixels by padding margins with zero, where $\xi_{a,b}$ denotes the (a, b)th pixel of the reshaped $\overline{\overline{\xi}}$. $\eta > 0$ is a small parameter to ensure that $f_{TV}(\overline{\overline{\xi}})$ is differentiable.

In minimizing the objective function (25), we alternatively update the coefficients $\overline{\alpha}_p$ and the polarization tensor $\overline{\overline{\xi}}$ with conjugate gradient (CG) method. The implementation procedures are as follows:

- Step 1) Initial step ($n = 0$ and $k = 1$): Initialize $\overline{\overline{\xi}} = 0$, $\overline{\alpha}_{p,0} = 0$, and $\overline{\rho}_{p,0} = 0$. (To increase the convergence speed, $\overline{\overline{\xi}}$ can also be initialized as $\overline{\overline{\xi}} = \overline{\overline{\xi}}_b$ with $\overline{\overline{\xi}}_b$ being the results of back propagation [42], [44].)
- Step 2) n=n+1. Update $\overline{\alpha}_{p,n}$: $\overline{\alpha}_{p,n} = \overline{\alpha}_{p,n-1} + d_{p,n}\overline{\rho}_{p,n}$, where $\overline{\rho}_{p,n}$ is the Polak-Ribière-Polyak (PRP) conjugate gradient [45] of objective function (25) with respect to $\overline{\alpha}_{p,n}$ and $d_{p,n}$ is the search length. It is noted that the objective function (25) is quadratic in terms of parameter $d_{p,n}$, and an optimal $d_{p,n}$ can be easily obtained [42].
- Step 3) Update $\overline{\overline{\xi}}_n$ ($h = 1$):
  - Step 3.1) Initialize $\overline{\overline{\xi}}_n$ as $\overline{\overline{\xi}}_{n,0}$: For the mth subunit, update the induced contrast current $(\overline{J}_{p,n})_m$ and the total electric filed $(\overline{E}_{p,n}^t)_m$ following (21) and (13), respectively. Then objective function (24) becomes quadratic in terms of $(\overline{\overline{\xi}}_n)_m$, and the solution is given by [13]:

$$(\overline{\overline{\xi}}_{n,0})_m = [\sum_{p=1}^{N_i} \frac{(\overline{E}_{p,n}^t)_m^*}{||\overline{J}_p^+||} \cdot \frac{(\overline{J}_{p,n})_m}{||\overline{J}_p^+||}] / [\sum_{p=1}^{N_i} | \frac{(\overline{E}_{p,n}^t)_m}{||\overline{J}_p^+||} |^2] \tag{27}$$

  - Step 3.2) Updated $\overline{\overline{\xi}}_{n,h}$ with $\overline{\overline{\xi}}_{n,h} = \overline{\overline{\xi}}_{n,h-1} + d_h\overline{\rho}_h$, where $\overline{\rho}_h$ is the PRP conjugate gradient of objective function (25) with respect to $\overline{\overline{\xi}}_{n,h}$ and d_h is the search length.
  - Step 3.3) Let $h = h + 1$. If the termination condition ($h > 20$ in this paper) is satisfied, stop iteration and go to step 4). Otherwise, go to step 3.2).
- Step 4) If the termination condition, such as n reaching the maximum iterations, is satisfied, stop iteration and go to step 5). Otherwise, go to step 2).
- Step 5) If $k = S$, stop iteration. Otherwise, let $k = k + 1$, $n = 0$, and go to step 2).

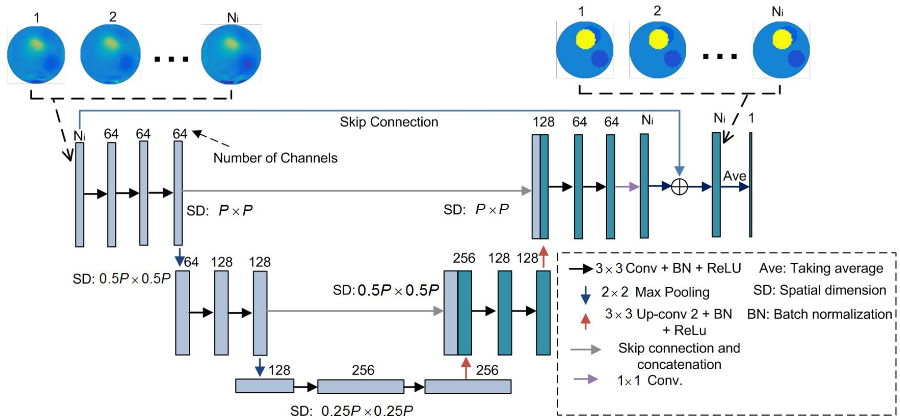

Fig. 2. The U-net architecture for the proposed DC-DLS. The details of U-net can be found in [29], [33]. An example of inputs and labels in training is also depicted on top of neural network.

B. Dominant-Current Deep Learning Scheme

The BE-SOM presented in Section III-A is an iterative reconstruction method. Many components of BE-SOM motivate us to propose a CNN model, namely DC-DLS, to reconstruct conductivity with a much faster speed. The proposed DC-DLS consists of three steps.

In the first step of DC-DLS, we turn our attention from directly computing conductivity to obtaining a dominant component of ICC, which is utilized to generate inputs of CNN. The dominant current have two features. The first one is that it contains most of the important features of the unknown objects, and the second is that it was found to be robust to measurement noise, such as Gaussian noises [38].

As mentioned just after (20), $\overline{J}_p^+$ contains the most important information of ICC, but it has missed some information contained in J_p^-. To compensate the missing information $\overline{J}_p^-$, we introduce the concept of dominant current $\overline{J}_p^d$, which consists of the major part of ICC $\overline{J}_p^+$ and a low-frequency current $\overline{J}_p^l$ with

$$\overline{J}_p^d = \overline{J}_p^+ + \overline{J}_p^l, \tag{28}$$

where the superscript d and l denotes dominant and low-frequency, respectively. The current $\overline{J}_p^l$ is represented by

$$\overline{J}_p^l = \overline{\overline{F}}_{M_1}^l \cdot \overline{\alpha}_p^l, \tag{29}$$

where $\overline{\overline{F}}_{M_1}^l$ and $\overline{\alpha}_p^l$ are low-frequency matrix in the first stage of (21) and its corresponding coefficients, respectively. The motivation of constructing $\overline{J}_p^d$ in (28) is that studies have shown that deep architecture properties of CNNs, namely their strong learning capability and high representational capacity, are well suited to image restoration from degraded inputs [46]. Thus, it is a good choice to exclude the high frequency part of ICC, which is easily contaminated by noises, and let CNNs to restore this part by training.

The second step of DC-DLS is to obtain the value of $\overline{\alpha}_p^l$. In this paper, $\overline{\alpha}_p^l$ is obtained from the first stage ($k=1$) of BE-SOM. Due to the significantly reduced number of unknowns at the first stage of BE-SOM, the convergence rate is very fast and $\overline{\alpha}_p^l$ can be obtained in a few seconds for typical EIT problems.

Then, the final step is to calculate the polarization tensor $\overline{\overline{\xi}}_p^d$ of DC-DLS based on $\overline{J}_p^d$. Specifically, according to (10), the total electrical field $\overline{E}_p^{t,d}$ in DC-DLS for the pth incidence can be updated as

$$\overline{E}_p^{t,d} = \overline{E}_p^0 + \overline{\overline{G}}_D \cdot \overline{J}_p^d. \tag{30}$$

Then, based on the definition

$$\overline{J}_p^d = \overline{\overline{\xi}}_p^d \cdot \overline{E}_p^{t,d}, \tag{31}$$

the mth element of the contrast $\overline{\overline{\xi}}_p^d$ for the pth incidence is obtained with

$$(\overline{\overline{\xi}}_p^d)_m = \frac{(\overline{J}_p^d)_m \cdot (\overline{E}_p^{t,d})_m^*}{||(\overline{E}_p^{t,d})_m||^2}. \tag{32}$$

In the learning process of DC-DLS, the conductivity obtained from the polarization tensor $\overline{\overline{\xi}}_p^d$ in (32) is assigned into different input-channels of CNN, and each corresponding output-channel is the true conductivity of the domain D. Consequently, there are N_i pairs of input- and output-channels of DC-DLS corresponding to a total number of N_i current injections.

It is seen in the derivations of DC-DLS that, the dominant part $\overline{J}_p^d$ of ICC contains most of the information from the data equation (18) and it is used to generate the input of CNN following (32). Since both input and output of the proposed neural network are data that are within the DOI D, DC-DLS

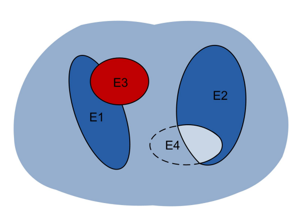

Fig. 3. Illustration of random-ellipse dataset, which consists of four randomly distributed ellipses.

TABLE I
RELATIVE ERRORS R_e FOR THE NUMERICAL EXAMPLES.

R_e	Phantom 1	Phantom 2	Phantom 3	Pneumothorax	Pleural Effusion
BE-SOM	0.118	0.16	0.14	0.15	0.15
DC-DLS (Input)	0.15	0.196	0.18	0.21	0.18
DC-DLS (Output)	0.09	0.087	0.098	0.12	0.14

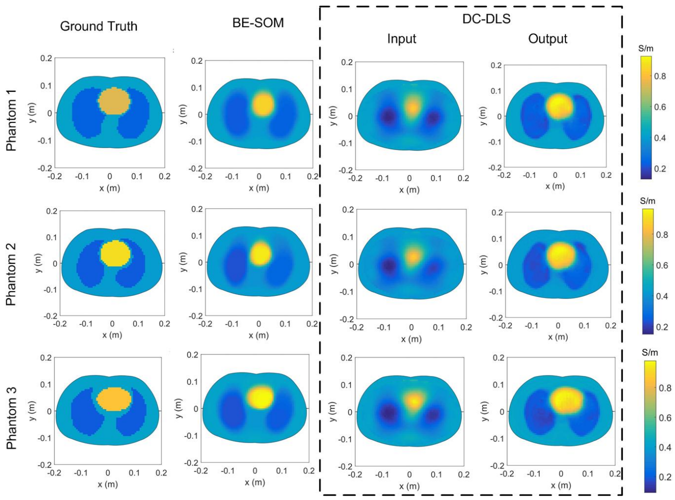

Fig. 4. Reconstructions of "heart and lung" phantoms: BE-SOM and DC-DLS are used to reconstruct conductivity distributions from collected voltages with 0.5% Gaussian noises (SNR=46 dB) presented. The "Input" column corresponds to the input images of the first channel in DC-DLS.

mainly trains and learns the EIT physics within DOI, i.e., the state equation (14). Further, by utilizing the known dominant parts of ICC as inputs, DC-DLS decreases the nonlinearity of the state equation and makes it easier for CNN in the learning process.

C. U-net Convolutional Neural Network

1) Architecture: In this work, U-net architecture, originally designed for segmentation [29] is used to implement the proposed DC-DLS. As presented in Fig. 2, the U-net architecture consists of a contracting path (left side) and an expansive path (right side). The contracting path consists of repeated application of 3×3 convolutions, batch normalization, and rectified linear unit (ReLU), which is followed by a 2×2 max pooling operation. The expansive path is similar to contracting path, but the max pooling in contracting path is replaced by a 3×3 up convolution in expansive path. In expansive path, there are also two concatenations with the correspondingly cropped feature maps from the contracting path. We choose the well-suited U-net architecture and modify the structure to solve the nonlinear EIT imaging problems:

- The downsampling in U-net significantly increase the receptive field of a unit in neural network, which is important for inverse problems in EIT since a large field of view over the input image can significantly improve the prediction at each pixel of the output image [47].
- A skip connection is inserted from the input of the neural network to its output layer in the U-net architecture used in the manuscript. This approach is particular well suited to the proposed DC-DLS since the inputs and outputs share similar important features. Specifically, the skip connection enforces the network learning the difference between the inputs and outputs, which avoids learning abundant part already contained in the inputs. In addition, this skip connection also mitigates the vanishing gradient problem during training [33], [36].
- Batch Normalization (BN) is used to alleviate the internal covariate shift, i.e., the change in the distribution of network activations due to the change in network parameters during training [37].
- We have applied a multiple-channel scheme (MCS) in DC-DLS. The MCS adopted in DC-DLS enlarges the data set by utilizing the information from all current injections and increases the robustness by taking average of all outputs in different channels.
- We have also incorporated different physical information into the inputs of the proposed DC-DLS. For example, the inputs of the DC-DLS are computed from a kind of induced contrast current, rather than the measured voltage. Namely, the input also provides a warm start to the CNN instead of directly using the measured voltage. This choice avoids the otherwise unnecessary computational effort of CNN spent on learning the physical mechanism (i.e., $\overline{\overline{G}}_\partial$ in (18)).

2) Training: In this work, we propose a training strategy to reconstruct "heart and lung" phantoms in EIT with random-ellipse dataset (RED). As depicted in Fig. 3, RED consists of four random distributed ellipses with random conductivities and sizes, which are marked as $E1$, $E2$, $E3$, and $E4$, respectively. The four ellipses are allowed to interlap with each other, and the conductivity in the latter ellipse will replace the one generated early, i.e., if $E3$ interlaps with $E1$, the conductivity of $E3$ will replace the conductivity of $E1$ in the interlapping region. In Fig. 3, $E1$ and $E2$ are allowed to rotate with random angles in $[-30°, 30°]$ and the conductivities of them are randomly chosen in the same range, which are used to model lungs. The detailed values of conductivity will be introduced in Section IV. In RED, $E3$ is used to model heart, and $E4$ is used to model possible deformations and pathologies in lung, thus it only presents in the interlapping region of $E4$ with $E1$ or $E2$. The details of training parameters, such as the ranges of radii and conductivities, will be introduced in Section IV. It is noted that RED is highly adaptive and not limited in training "heart and lung" phantoms since both the number of random ellipses and parameter ranges can be changed according to practical applications.

The cost function used for training in DC-DLS is Euclidean

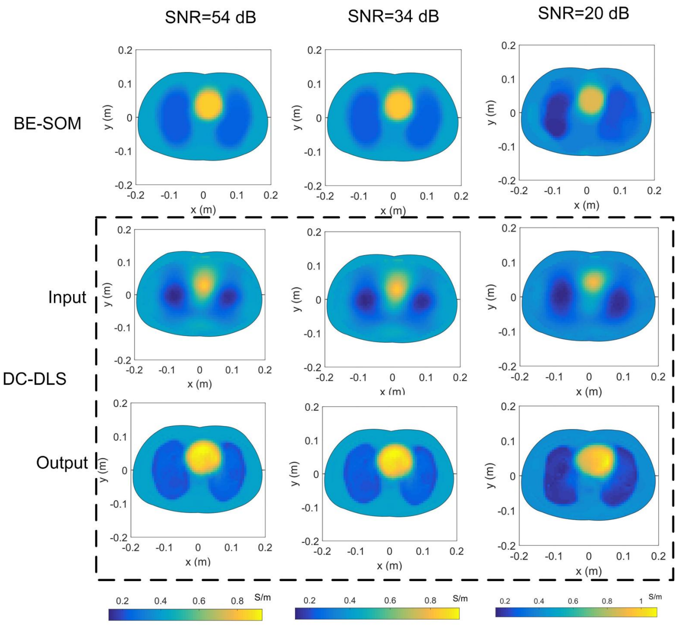

Fig. 5. Reconstructions of Phantom 1 with different noise levels: Left, middle, and right columns correspond to 0.2% (SNR=54 dB), 2% (SNR=34 dB), and 10% (SNR=20 dB) Gaussian noises, respectively.

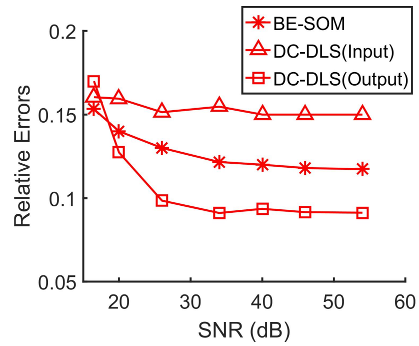

Fig. 6. Trajectories of relative errors in reconstructing Phantom 1 as a function of SNR.

loss. MatConvNet toolbox [48] is used to implement the proposed CNN scheme. The hyperparameters for the network in training in DC-DLS are as follows: learning rate decreasing logarithmically from 10^{-6} to 10^{-8}; momentum equals 0.99; weight decay equals to 10^{-6}. We empirically applied an "early stopping" strategy to mitigate the effect brought by overfitting. Specifically, we empirically stop the training at a position where validation loss shows apparent divergence with training loss. Adding more data in training will also help in dealing with overfitting issues if more powerful hardware is available

3) Testing: In this work, profiles of numerical tests consist of three "heart and lung" phantoms and 40 synthetic tests from RED. The profiles of the three phantoms with random conductivities are presented in Fig. 4. In the tests with experimental data, we test BE-SOM and the trained network in DC-DLS on conductive and resistive targets with various shapes measured by the KIT4 (Kuopio Impedance Tomography) EIT system [49].

IV. Numerical Results

A. Implementation Details

In this section, as presented in Fig. 1, we study reconstructions from simulated voltages collected on chest-shaped domain with perimeter 106.4 cm. $N_r = 32$ electrodes with the width of $w_e = 2.5$ cm are attached on the boundary $\partial\Omega$, and the background is saline with the conductivity $\sigma_0 = 0.424$ S/m. We consider a commonly used trigonometric current patterns (TCPs) which sinusoidal patterns are applied on all electrodes and the resulting voltages are measured on all electrodes. Specifically, $N_i = 16$ current patterns are applied with the formulae for TCPs are

$$J_q^{2t-1} = J_0 \cos(t\theta_q) \tag{33}$$

and

$$J_q^{2t} = J_0 \sin(t\theta_q), \tag{34}$$

with $\theta_q = 2\pi q/N_r$, $J_0 = 0.125$ mA/cm, q=1, 2, …, N_r, and $t = 1, 2, \ldots, N_i/2$.

In this section, we consider an ellipse-shaped DOI D with long radius 18 cm and short radius 12 cm centered at the central point of the chest. In discretization, the DOI is divided into $M = 1739$ subunits, each with dimensions 0.625 cm $\times$ 0.625 cm. The measured voltage is computed by MOM with a different mesh to avoid inverse crime, and recorded as a matrix $\overline{\overline{R}}$ with the size of $N_r \cdot N_i$. In the training process, noiseless voltages are used, whereas for all the numerical tests, additive white Gaussian noise $\overline{\overline{n}}$ is added to the measured voltages. The noise level is quantified by $N_l = (||\overline{\overline{n}}||_F/||\overline{\overline{R}}||_F)$ with $||\cdot||_F$ denoting Frobenius norm, and the signal to noise ratio (SNR) in dB is consequently calculated as $\mathrm{SNR} = 20\log_{10}(1/N_l)$.

In order to quantitatively evaluate the performance of different schemes, a relative error R_e is also defined as

$$R_e = ||\overline{\overline{\sigma}}^t - \overline{\overline{\sigma}}^r||_F/||\overline{\overline{\sigma}}^t||_F, \tag{35}$$

where $\overline{\overline{\sigma}}^t$ and $\overline{\overline{\sigma}}^r$ are true and reconstructed conductivity profiles, respectively. It is noted that, in the reconstruction process, we have added the constraint that values of conductivity are positive, which is an obvious physical fact. For the empirical parameters L in BE-SOM and DC-DLS, a successive range of integer L ($8 \le L \le 25$ in this paper), instead of a single one, works for a reconstruction problem. In this paper, we use $L = 15$ following the suggestions in the previous literature [13]. For BE-SOM, $S = 3$ stages with $M_1 = 10 \times 10$, $M_2 = 20 \times 20$, and $M_3 = 39 \times 39$ are applied throughout this section. For all examples in this section, the weighting parameters of total variation (β) are chosen as 0, 0.01, and 0.01 for the three stages, respectively. Specifically, $\beta = 0$ is chosen at the first stage so that objective function f_d in (25) is reduced fast when the results are not accurate at the beginning of optimizations, and $\beta = 0.01$ is chosen for the other stages empirically to make sure that the objective function f_d and f_{TV} in (25) are in the same order of magnitude. A maximum iterations of 150 are set for each stage unless there are no apparent changes in the objective function (differential value between two consecutive objective function in iterations is smaller than 10^{-3}). According to our observations, around

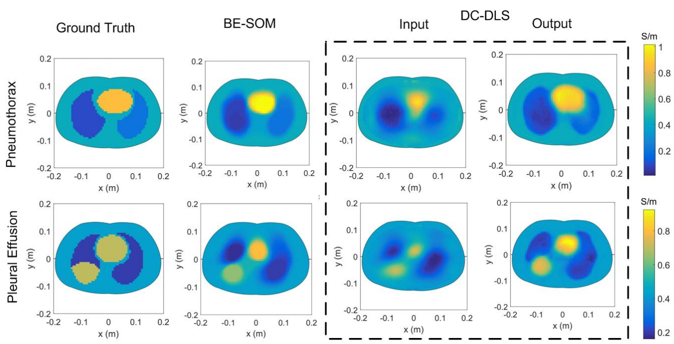

Fig. 7. Reconstructions of pneumothorax and pleural effusion pathologies in "heart and lung" phantoms, where 0.5% Gaussian noises (SNR=46 dB) are presented in the collected voltages.

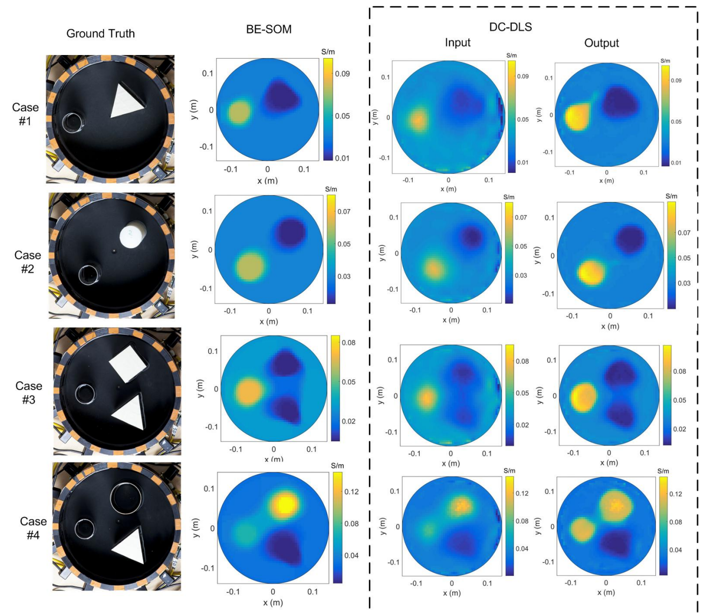

Fig. 8. Reconstructions of conductive and resistive targets measured on the KIT4 (Kuopio Impedance Tomography) EIT system. The white objects are made of solid plastic and are resistive, and the hollow circular objects are conductive metal rings [49].

50 iterations are sufficient for the first two stages since the number of unknowns is much smaller than that in the last stages.

In all the tests, the RED is synthetically generated comprising 800 images consisting of random ellipses with random conductivities. Among the 800 profiles, 760 of them are used to train CNNs with the proposed DC-DLS, and 40 images are used to test the trained CNN. The parameters in the RED for numerical sections are set as follows: The vertical and horizontal radii for both $E1$ and $E2$ are randomly chosen in the ranges 6-10 cm and 4-7 cm, respectively, where the conductivities are randomly chosen between 0.1 S/m and 0.3 S/m. Both the vertical and horizontal radii for $E3$ and $E4$ are randomly chosen in the range 2-6 cm, where the conductivities of $E3$ are randomly chosen between 0.6 S/m and 1 S/m. The conductivities of $E4$ are randomly chosen between 0 S/m and 1 S/m to model possible pathologies on lungs ($E1$ and $E2$), where the conductivities of 30% numbers of $E4$ in RED are made as background conductivity to model possible deformations on lungs. It is noted that, before inputting into CNN, the conductivity distributions obtained from (32) are reshaped to $P \times P$ pixels by padding margins with background conductivity σ_0, where $P = 64$ is used in all the numerical tests.

To fairly compare the time consumed in each example, for all reconstructions, we use personal computer with CPU (3.4 GHz Intel Core i7 Processor and 16 GB RAM). For a training with 40 epoches in DC-DLS, it takes about 2.1 hours, which varies slightly for different examples. It is noted that, since each operation of CNN is simple and local, both the training and test processes are ideal for GPU-based parallelization. Consequently, the time spent on DC-DLS can be further reduced by GPU calculation.

B. Examples of Reconstructions

In the first example, three different "heart and lung" phantoms are considered, where the ground truth of conductivity distributions are presented in the first column of Fig. 4. The conductivities are randomly chosen from the ranges introduced in the previous section. In Fig. 4, reconstructed results from the proposed BE-SOM and DC-DLS are presented, where 0.5% Gaussian noises (SNR=46 dB) are added in the collected voltages. Here, all images are shown in DICOM orientation in which the left lung is on the viewer's right [20]. It is found from Fig. 4 that both BE-SOM and DC-DLS can distinguish some small but important features in the three phantoms, such as the curves at the connection part of lung and heart in phantom 1, the relative small size of left lung in Phantom 2, and the rotation of lungs in Phantom 3. Despite the fact that these small features can hardly simultaneously included in the four random-ellipses training data, DC-DLS still shows satisfying results for all these small features. Further, compared with BE-SOM, it is seen that the reconstructed images of DC-DLS have much shaper boundaries, and the reason is that the large number of training data offers strong constraints for CNN scheme. To quantitatively compare the results, relative errors R_e are computed and shown in Table I. It suggests that DC-DLS quantitatively outperforms BE-SOM for all the three Phantom tests in terms of reconstructed image qualities.

To validate the robustness of the proposed method to noises, reconstructions are also conducted on Phantom 1 from voltages contaminated by Gaussian noises with different noise levels. As presented in Fig. 5, it is seen that both the proposed methods are robust to noises, and the profiles of Phantom 1 are reconstructed even with 2% (SNR=34 dB) noises presented. It can also be found from Fig. 5 that, with a very large noise level (SNR=20 dB), some discrepancies are shown on results from the proposed methods. To further quantitatively evaluate the effects of noise contaminations on the proposed methods, the relative of errors varying with different noise levels are also presented in Fig. 6.

In the second example, we consider two phantoms with different pathologies including pneumothorax and pleural effusion depicted in Fig. 7, where pneumothorax and pleural effusion show regions with apparent lower and higher conductivities than those of healthy lungs, respectively. To better evaluate the proposed method, we have intensionally put those pathologies in different portions of lungs for different phantoms. It is seen from Fig. 7 that, both pneumothorax and pleural effusions are clearly visible in the reconstructions for the proposed BE-SOM and DC-DLS. To quantitatively compare the reconstructed results, the relative errors are also computed and compared in Table I, where smaller relative errors are observed for DC-DLS in all the tests.

V. Tests with Experimental Data

To further validate the proposed methods, tests with BE-SOM and DC-DLS have also been conducted with experimental data collected on the four scenarios shown in Fig. 8. The experiments were conducted using a tank of circular cylinder shape with the radius of $R_t = 14$ cm. Sixteen rectangular electrodes (height 7 cm, width 2.5 cm) were attached equidistantly on the inner surface of the tank. The tank was filled with saline with the measured conductivity of 0.03 S/m, and $N_i = 16$ adjacent current injections were applied with an amplitude of 2 mA [49]. Conductive and resistive targets were presented in the tank and voltages were measured on the KIT4 (Kuopio Impedance Tomography) EIT system.

In the reconstructions, we consider a circular DOI D with a radius of $0.95R_t$ centered at the central point of saline tank. In discretization, the DOI is divided into $M = 1696$ subunits with dimensions 0.571 cm $\times$ 0.571 cm. In the training of DC-DLS, we use only random circular data. Specifically, one to three circular inclusions are simulated with random radii varying from 1 cm to 6 cm and the circular inclusions are allowed to interlap with each other to model possible complex inclusions. Following the settings in [21], the conductivities values are assigned in two ranges ([0.05, 0.12] S/m and [0.005, 0.015] S/m) to model "conductive" and "resistive", respectively. Before being used as the inputs of CNN, the conductivity distributions obtained from (32) are reshaped to $P \times P$ pixels with $P = 52$ by padding margins with background conductivity σ_0 =0.03 S/m. For BE-SOM, $S = 3$ stages with $M_1 = 10 \times 10$, $M_2 = 20 \times 20$, and $M_3 = 46 \times 46$ are applied in all scenarios. The weighting parameters of total variation (β) for all scenarios are chosen as 0, 10, and 10 for the three stages, respectively, where we we follow the criterion introduced in Section IV-A. Namely, at the beginning of optimizations, $\beta = 0$ is chosen to make sure the objective function f_d in (25) is reduced fast when the results are not accurate, and $\beta = 10$ is chosen for the other stages empirically to make sure that the objective function f_d and f_{TV} in (25) are in the same order of magnitude. All other parameters are the same as those in numerical section.

In Fig. 8, we present the reconstructed results from the measured voltages with BE-SOM and DC-DLS. In each scenario, the time spent on reconstruction for BE-SOM and DC-DLS are 61 s and 8 s, respectively. It is found that both the proposed methods obtain satisfying results even for some challenging inclusions, such as triangular and rectangular shapes. Although the network is trained with only circular inclusions, the proposed DC-DLS is able to reconstruct triangular and rectangular inclusions, which highly improves the applicable ranges of the deep learning on EIT imaging.

VI. Conclusion

In this work, we proposed an iterative-based inversion method and a CNN-based inversion method for EIT applications. The proposed iterative-based inversion method, namely the bases-expansion subspace optimization method (BE-SOM), introduces the concept of induced contrast current (ICC) in EIT problem. These concepts are essential for us to apply a method of moment (MOM) under the gap model. Reconstructions are conducted on chest-shaped domain for several realistic phantoms including pneumothorax and pleural effusion pathologies. The theoretical analysis of BE-SOM and the physical concepts introduced there motivate us to propose a deep learning scheme (DC-DLS). By utilizing the dominant parts of ICC, DC-DLS trains and learns the mathematical relationship between ground-truth conductivities and the conductivities that are obtained from the dominant part of ICC in the natural pixel bases, which describes the EIT physics within the domain of interest. It was demonstrated that the proposed DC-DLS significantly improves the applicable ranges of deep learning on EIT imaging. Reconstructed results from both numerical and experimental data also show that both DC-DLS and BE-SOM are capable of fast, high-quality and stable imaging in EIT.

It is important to stress that the proposed approach not only allows to reconstruct the contrast, i.e., conductivity change in general difference EIT when the measurement data before the change is available, but also offers a chance to estimate the absolute conductivity distribution. Finally, we mention in passing that although the presentation of this work is given in a 2D context, an extension of the proposed frameworks to 3D is straightforward, where similar extensions have been verified in inverse scattering problems [50].

In addition, more advanced CNN architectures may yield better results with the proposed ICC framework, such as adversarial learning. The performance may also be improved by incorporating spatial *a priori* information into the training process. To sum up, the proposed method is promising in providing quantitative images for potential clinical applications, such as monitoring health condition of lungs.

References

[1] P. Metherall *et al.*, "Three-dimensional electrical impedance tomography," *Nature*, vol. 380, p. 509, 1996.

[2] K. Jihyeon, W. Eung Je, and S. Jin Keun, "Multi-frequency time-difference complex conductivity imaging of canine and human lungs using the KHU mark1 EIT system," *Physiological Measurement*, vol. 30, no. 6, p. S149, 2009.

[3] L. Borcea, "Electrical impedance tomography," *Inverse Problems*, vol. 18, no. 6, p. R99, 2002.

[4] A. Adler and A. Boyle, "Electrical impedance tomography: Tissue properties to image measures," *IEEE Transactions on Biomedical Engineering*, vol. 64, no. 11, pp. 2494–2504, 2017.

[5] A. Sujin *et al.*, "Validation of weighted frequency-difference EIT using a three-dimensional hemisphere model and phantom," *Physiological Measurement*, vol. 32, no. 10, p. 1663, 2011.

[6] I. Frerichs *et al.*, "Regional lung perfusion as determined by electrical impedance tomography in comparison with electron beam CT imaging," *IEEE Transactions on Medical Imaging*, vol. 21, no. 6, pp. 646–652, 2002.

[7] H. J. Smit *et al.*, "Determinants of pulmonary perfusion measured by electrical impedance tomography," *European Journal of Applied Physiology*, vol. 92, no. 1, pp. 45–49, 2004.

[8] G. Alessandrini and S. Vessella, "Lipschitz stability for the inverse conductivity problem," *Advances in Applied Mathematics*, vol. 35, no. 2, pp. 207–241, 2005.

[9] D. Liu *et al.*, "Nonlinear difference imaging approach to three-dimensional electrical impedance tomography in the presence of geometric modeling errors," *IEEE Transactions on Biomedical Engineering*, vol. 63, no. 9, pp. 1956–1965, 2016.

[10] Z. Zhou *et al.*, "Comparison of total variation algorithms for electrical impedance tomography," *Physiological Measurement*, vol. 36, no. 6, p. 1193, 2015.

[11] A. K. Khambampati *et al.*, "Boundary element method to estimate the time-varying interfacial boundary in horizontal immiscible liquids flow using electrical resistance tomography," *Applied Mathematical Modelling*, vol. 40, no. 2, pp. 1052–1068, 2016.

[12] L. Borcea, G. A. Gray, and Y. Zhang, "Variationally constrained numerical solution of electrical impedance tomography," *Inverse Problems*, vol. 19, no. 5, pp. 1159–1184, 2003.

[13] X. Chen, "Subspace-based optimization method for solving inverse-scattering problems," *IEEE Transactions on Geoscience and Remote Sensing*, vol. 48, no. 1, pp. 42–49, 2010.

[14] ——, "Subspace-based optimization method in electric impedance tomography," *Journal of Electromagnetic Waves and Applications*, vol. 23, no. 11-12, pp. 1397–1406, 2009.

[15] B. Harrach, J. K. Seo, and E. J. Woo, "Factorization method and its physical justification in frequency-difference electrical impedance tomography," *IEEE Transactions on Medical Imaging*, vol. 29, no. 11, pp. 1918–1926, 2010.

[16] N. Chaulet *et al.*, "The factorization method for three dimensional electrical impedance tomography," *Inverse Problems*, vol. 30, no. 4, p. 045005, 2014.

[17] A. P. Calderón, "On an inverse boundary value problem," *Computational & Applied Mathematics*, vol. 25, pp. 133–138, 2006.

[18] P. A. Muller, J. L. Mueller, and M. M. Mellenthin, "Real-time implementation of calderón's method on subject-specific domains," *IEEE Transactions on Medical Imaging*, vol. 36, no. 9, pp. 1868–1875, 2017.

[19] D. Isaacson *et al.*, "Reconstructions of chest phantoms by the D-bar method for electrical impedance tomography," *IEEE Transactions on Medical Imaging*, vol. 23, no. 7, pp. 821–828, 2004.

[20] S. J. Hamilton, J. L. Mueller, and M. Alsaker, "Incorporating a spatial prior into nonlinear D-bar EIT imaging for complex admittivities," *IEEE Transactions on Medical Imaging*, vol. 36, no. 2, pp. 457–466, 2017.

[21] S. J. Hamilton and A. Hauptmann, "Deep D-bar: Real time electrical impedance tomography imaging with deep neural networks," *IEEE Transactions on Medical Imaging*, pp. 1–1, 2018.

[22] D. Liu *et al.*, "A nonlinear approach to difference imaging in eit; assessment of the robustness in the presence of modelling errors," *Inverse Problems*, vol. 31, no. 3, p. 035012, 2015.

[23] V. Kolehmainen *et al.*, "Assessment of errors in static electrical impedance tomography with adjacent and trigonometric current patterns," *Physiological Measurement*, vol. 18, no. 4, p. 289, 1997.

[24] A. Krizhevsky, I. Sutskever, and G. E. Hinton, "Imagenet classification with deep convolutional neural networks," pp. 1097–1105, 2012.

[25] O. Russakovsky *et al.*, "Imagenet large scale visual recognition challenge," *International Journal of Computer Vision*, vol. 115, no. 3, pp. 211–252, 2015.

[26] G. Cheng, C. Yang, X. Yao, L. Guo, and J. Han, "When deep learning meets metric learning: Remote sensing image scene classification via learning discriminative cnns," *IEEE Transactions on Geoscience and Remote Sensing*, vol. 56, no. 5, pp. 2811–2821, 2018.

[27] J. Han, D. Zhang, G. Cheng, N. Liu, and D. Xu, "Advanced deep-learning techniques for salient and category-specific object detection: A survey," *IEEE Signal Processing Magazine*, vol. 35, no. 1, pp. 84–100, 2018.

[28] R. Girshick *et al.*, "Rich feature hierarchies for accurate object detection and semantic segmentation," pp. 580–587, 2014.

[29] O. Ronneberger, P. Fischer, and T. Brox, "U-net: Convolutional networks for biomedical image segmentation," in *Medical Image Computing and Computer-Assisted Intervention MICCAI 2015: 18th International Conference*, 2015, pp. 234–241.

[30] J. Xie, L. Xu, and E. Chen, "Image denoising and inpainting with deep neural networks," in *Proceedings of the 27th International Conference on Neural Information Processing Systems*, 2012, pp. 341–349.

[31] L. Xu, J. S. J. Ren, C. Liu, and J. Jia, "Deep convolutional neural network for image deconvolution," in *Proceedings of the 27th International Conference on Neural Information Processing Systems*, 2014, pp. 1790–1798.

[32] C. Dong *et al.*, "Image super-resolution using deep convolutional networks," *IEEE Transactions on Pattern Analysis and Machine Intelligence*, vol. 38, no. 2, pp. 295–307, 2016.

[33] K. H. Jin *et al.*, "Deep convolutional neural network for inverse problems in imaging," *IEEE Transactions on Image Processing*, vol. 26, no. 9, pp. 4509–4522, 2017.

[34] A. F. Peterson, S. L. Ray, and R. Mittra, *Computational methods for electromagnetics*. Wiley-IEEE Press New York, 1998, vol. 2.

[35] E. Somersalo *et al.*, "Existence and uniqueness for electrode models for electric current computed tomography," *SIAM Journal on Applied Mathematics*, vol. 52, no. 4, pp. 1023–1040, 1992.

[36] K. He, X. Zhang, S. Ren, and J. Sun, "Deep residual learning for image recognition," in *2016 IEEE Conference on Computer Vision and Pattern Recognition (CVPR)*, 2016, pp. 770–778.

[37] S. Ioffe and C. Szegedy, "Batch normalization: Accelerating deep network training by reducing internal covariate shift," in *in Proc. Int. Conf. Mach. Learn.*, 2015, p. 448456.

[38] Z. Wei and X. Chen, "Deep-learning schemes for full-wave nonlinear inverse scattering problems," *IEEE Transactions on Geoscience and Remote Sensing*, Accepted, 2018.

[39] J. Jackson, *Classical Electrodynamics*. Wiley, 1998.

[40] Y. Zhong and X. Chen, "MUSIC imaging and electromagnetic inverse scattering of multiple-scattering small anisotropic spheres," *IEEE Transactions on Antennas and Propagation*, vol. 55, no. 12, pp. 3542–3549, 2007.

[41] K. Agarwal and X. Chen, "Applicability of MUSIC-Type imaging in two-dimensional electromagnetic inverse problems," *IEEE Transactions on Antennas and Propagation*, vol. 56, no. 10, pp. 3217–3223, 2008.

[42] X. Chen, *Computational Methods for Electromagnetic Inverse Scattering*. Wiley, 2018.

[43] P. L. Combettes and L. Jian, "An adaptive level set method for nondifferentiable constrained image recovery," *IEEE Transactions on Image Processing*, vol. 11, no. 11, pp. 1295–1304, 2002.

[44] K. Belkebir, P. C. Chaumet, and A. Sentenac, "Superresolution in total internal reflection tomography," *Journal of the Optical Society of America A*, vol. 22, no. 9, pp. 1889–1897, 2005.

[45] Y. H. Dai and Y. Yuan, "A nonlinear conjugate gradient method with a strong global convergence property," *Siam Journal on Optimization*, vol. 10, no. 1, pp. 177–182, 1999.

[46] R. Wang and D. Tao, "Non-local auto-encoder with collaborative stabilization for image restoration," *IEEE Transactions on Image Processing*, vol. 25, no. 5, pp. 2117–2129, 2016.

[47] J. Justin, A. Alexandre, and F.-F. Li, "Perceptual losses for real-time style transfer and super-resolution," in *in Proc. European Conf. Computer Vision*. Cham: Springer International Publishing, 2016, pp. 694–711.

[48] A. Vedaldi and K. Lenc, "Matconvnet: Convolutional neural networks for matlab," in *Proc. ACM Int. Conf. Multimedia*, 2015, pp. 689–692.

[49] A. Hauptmann *et al.*, "Open 2d electrical impedance tomography data archive," *arXiv preprint arXiv: 1704.01178*, 2017.

[50] Y. Zhong and X. Chen, "An FFT twofold subspace-based optimization method for solving electromagnetic inverse scattering problems," *IEEE Transactions on Antennas and Propagation*, vol. 59, no. 3, pp. 914–927, 2011.